Journal of Materials Chemistry C

Accepted Manuscript

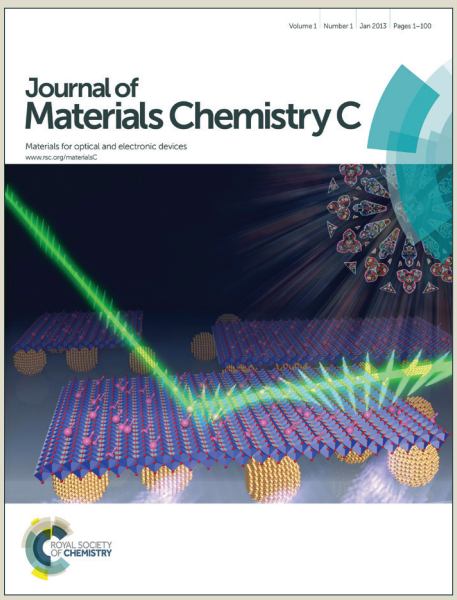

ROYAL SOCIETY OF CHEMISTRY

www.rsc.org/materialsC

Journal Name

RSCPublishing

ARTICLE

Inducing glassy magnetism in Co-ferrite nanoparticles through crystalline nanostructure

Cite this: DOI: 10.1039/x0xx00000x

Received ooth January 2012,
Accepted ooth January 2012

DOI: 10.1039/x0xx00000x

www.rsc.org/

Moya Carlos,[*a] Salas Gorka,[b,c] Morales María del Puerto,[b] Batlle Xavier[a] and Labarta Amílcar[a]

This work reports on the study of three samples of 8 nm Co-ferrite particles prepared by standard methods based on the thermal decomposition of metalorganic precursors. Although all samples are single phase according to conventional techniques of structural and chemical characterization, they show strongly sample-dependent magnetic properties ranging from bulk-like ferrimagnetism to glassy magnetic behaviour. We show that the presence of crystallite domains associated with crystallographic defects throughout the particles leads to highly-frustrated ferrimagnetic cores that are responsible for the glassy phenomenology, while only samples almost free of structural imperfections show bulk-like magnetic properties. These results suggest the key role of the crystal quality on the large variability of magnetic properties previously reported for Co-ferrite nanoparticles. Besides, getting control of the amount of structural defects in monodisperse, stoichiometric Co-ferrite nanoparticles can be an additional nano-structuring procedure to tailor their final magnetic properties.

Introduction

Magnetic nanomaterials are extensively studied at present because of the wealth of new phenomena occurring at the nanoscale. Among them magnetic nanoparticles (NPs) are excellent examples of nanosystems providing a plethora of either tailored or enhanced properties with respect to those of their bulk counterparts.[1] Particularly, ferrite nanoparticles with composition MFe_2O_4 (M = Fe, Co) are currently attracting a lot of interest due to their potential applications in biomedicine, such as the detection of biomolecules by magnetic separation, contrast improvement in nuclear magnetic resonance imaging and the cancer treatment by magnetic hyperthermia.[2-5] Co-ferrite NPs are especially suitable for those applications because of their high values of the magnetocrystalline anisotropy, saturation magnetization and the magneto-optical coefficients.[6] In addition, Co-ferrite NPs show a high magnetic response.

However, once size is reduced to the nanometer scale, NPs display particle-like magnetic behavior including finite-size effects such as superparamagnetism, oddly shaped hysteresis loops, and glassy behavior, among others.[1] In addition, there might be a breakdown of the usual scaling laws linking magnetic properties to size.[1] These effects are due to the influence of the particle surface on magnetic order via bond breaking and charge rearrangement, and to the closeness of the particle size to critical magnetic length scales like the domain wall width and spin-exchange length.[7] Besides, in spinel ferrite NPs, structural modifications at the grain boundaries and other crystallographic defects may provoke destabilization of the ferrimagnetic order yielding a variety of non collinear magnetic structures that become frozen in a kind of glassy state at low temperature.[8] The most important features characterizing this glassy state comprise the existence of high-field irreversibility in the magnetization curves, occurrence of shifted hysteresis loops after field cooling, reduction of the coercive field and the increase in the magnetic viscosity.[9] In the case of spinel ferrites such as $Co_xFe_{3-x}O_4$, further complexity arises due to the likely size-dependent cation distribution of the tetrahedral and octahedral sites in the close-packed oxygen structure, which strongly affects their saturation magnetization and magnetic anisotropy.[10] All the foregoing could cause the strongly sample-dependent magnetic properties that have been previously reported for Co-ferrite NPs, suggesting that the synthesis is affected by a number of factors limiting the reproducibility and crystal quality of the final samples.[11-13] The crucial role of the structural quality on the magnetic properties of the Co-ferrite NPs is thus proposed since only NPs almost free of structural defects show the magnetic performance suitable for many applications.[14] At the same time, getting control of the amount of structural defects in monodisperse, stoichiometric Co-ferrite NPs can be an additional nano-structuring procedure to tailor

their final magnetic properties. In this framework, we have addressed these issues by studying various samples of Co-ferrite NPs prepared by high-temperature decomposition of metalorganic precursors in an organic solvent with distinct reactants, in order to establish the close relationship between the actual magnetic behaviour and structural properties of the NPs. We have shown that samples with composition corresponding to stoichiometric Co-ferrite exhibit a wide variety of magnetic phenomena ranging from almost perfect bulk-like ferrimagnetic order with high coercive fields for Co-ferrite NPs of high crystallinity, to glassy magnetic behaviour for the most structurally defective samples. Interestingly enough,

Experimental details

Preparation of the samples

Three samples of Co-ferrite NPs were synthesized by high-temperature decomposition of various Fe and Co organic precursors in 1-octadecenne, using oleic acid as a surfactant in all cases and following standard methods reported elsewhere.[15-21] Metal oleates, used as organic precursors, were prepared from the reaction of the corresponding metal chlorides, $CoCl_2.6H_2O$ (Sigma-Aldrich, 99%), $FeCl_3.6H_2O$ (Sigma-Aldrich, 98%) and sodium oleate (Riedel-deHaën, 85%). Co-ferrite nanoparticles were prepared from oleate precursors of Fe and Co, iron(III) acetylacetonate (Sigma-Aldrich, 99%), cobalt(II) acetylacetonate (Sigma-Aldrich, 97%), 1,2-hexadecanediol (Sigma-Aldrich, 90%), oleic acid (Sigma-Aldrich 90%), oleylamine (Sigma- Aldrich 70%) and 1-octadecene (Sigma-Aldrich 90%). All reactants were used in the synthesis without further purification.

Synthesis of metal oleates. Cobalt (II) oleate. $CoCl_2.6H_2O$ (9.60 g, 40 mmol) was mixed with sodium oleate (32.60 g, 88 mmol) in a mixture of ethanol, distilled water and hexane (80 mL each). The reaction mixture was kept for 15 minutes under vigorous stirring. Then, the aqueous phase was removed and the organic phase was washed four times with a mixture of water and ethanol. Then, the organic solvent was removed and the Co(II) oleate was dried in a rotary evaporator. The resulting product was a purple solid.

Iron (III) oleate. For the synthesis of iron(III) oleate, $FeCl_3.6H_2O$ (10.80 g, 40 mmol) and sodium oleate (45.00 g 148 mmol) were dissolved in a mixture of distilled water, ethanol and hexane (60, 80 and 140 mL, respectively). The resulting solution was heated at 70 °C for 4 h under reflux. When the reaction was completed, organic products were washed three times with distilled water. Finally, hexane was removed in vacuum resulting in a waxy black solid.

Cobalt (II) Iron (III) oleate. The mixed-metal compound $Co^{2+}Fe_2^{3+}$-oleate was prepared by dissolving sodium oleate (23.76 g, 64 mmol), $CoCl_2.6H_2O$ (1.90 g, 8 mmols) and $FeCl_3.6H_2O$ (4.41 g, 16 mmols) in a mixture of water, ethanol and hexane (40, 40 and 80 mL, respectively). The reaction mixture was stirred and refluxed at 60 ºC for 4 h. Then, the aqueous phase was removed and the organic phase was washed three times with a mixture of ethanol and distilled water. A viscose brown liquid was obtained after evaporation of the hexane and ethanol at 100ºC.

Preparation of Co-ferrite NPs. Sample R1. Co and Fe acetylacetonates as metallic precursors: $Co(acac)_2$ (0.26 g, 1 mmol), $Fe(acac)_3$ (0.71 g, 2 mmol), 1,2-hexadecanediol (2.87 g, 10 mmol), oleic acid (1.88 g, 6 mmol) and oleylamine (2.29 g,6 mmol) were added to 1-octadecenne (20 mL). The mixture was heated at 200 ºC for 2 h under stirring in a flow of nitrogen gas. Then, the solution was heated up to reflux for 1 h. After that, the solution was cooled down to room temperature and transferred to 50 mL centrifugation tube together with 20 mL mixture of 2-propanol and ethanol with a volume ratio of 1:3. After three times of centrifugation at 9000 rpm for 15 min, a black powder was obtained, which was then dispersed in hexane for storage.

Sample R2. Co and Fe oleates as metallic precursors: A mixture of $Co(oleate)_2$ (0.62 g, 1 mmol), $Fe(oleate)_3$ (1.79 g, 2 mmol) and oleic acid (2.59 g, 9 mmol) were slowly heated under nitrogen atmosphere in 1-octadecene (20 mL) up to 80 ºC. Then, the solution was quickly heated up to reflux temperature for 1 h. The reaction mixture was washed with a mixture of 2-propanol and ethanol with a ratio of 1:3, and centrifuged. The procedure was repeated several times, until a clear solution was obtained. After that, the reaction product was re-dispersed in hexane.

Sample R3. Co and Fe acetylacetonates as metallic precursors: $Fe(acac)_3$ (0.71 g, 2mmol), $Co(acac)_2$ (0.26 g, 1 mmol) and oleic acid (2.59 g, 9 mmol) were mixed in 1-octadecene (20 mL). As for R1, after heating up to 200 ºC and staying at this temperature for 2 h, the solution was heated to reflux temperature, cooled down to room temperature and washed several times with a mixture of hexane and acetone with a volume ratio 1:3, and, finally, NPs were collected by centrifugation at 8000 rpm.

Experimental techniques

Particle shape and size were determined by transmission electron microscopy (TEM) using a MT80-Hitachi microscope. To get a deeper insight into the crystal quality and stoichiometry of individual NPs, high resolution TEM (HRTEM) images were obtained by Titan high-base. Electron energy loss spectroscopy (EELS) and energy-dispersive X-ray spectroscopy (EDX) data, both techniques with a spatial resolution of about 1 nm, were recorded by Titan low-base. TEM samples were prepared by placing a drop of a diluted suspension of NPs in hexane on a carbon-coated copper grid and further evaporation of the solvent at room temperature. Particle size distributions were determined by measuring at least 2000 particles for each sample and the resultant histograms are shown in Figure S1 in Supporting Information.

Crystal structures were identified by X-ray powder diffraction performed in a PANalytical X'Pert PRO MPD diffractometer by using Cu Kα radiation. The patterns were collected within 5 and 100º in 2θ. In all cases, the XRD spectra

were indexed to an inverse spinel structure. The mean particle diameters obtained from XRD (D_{XRD}) are given in Table 1.

The Fe and Co contents in the samples were determined by inductively coupled plasma-optical emission spectrometry (ICP-OES) by using a Perkin Elmer model OPTIMA 3200RL after digesting the samples in a mixture of HCl:HNO_3; 5:25, and finally diluting them with distilled water.

The organic fractions of the samples - Co and Fe acetylacetonates or oleates - were evaluated by thermogravimetric analysis (TGA). Measurements were performed in a TGA-SDTA 851e/SF/1100 (Mettler Toledo) at a heating rate of 10 ºC min^{-1} in nitrogen atmosphere from room temperature up to 800 ºC.

DC magnetization measurements were performed with a Quantum Design SQUID magnetometer. Hysteresis loops $M(H)$ were measured under a maximum applied field of ± 50 kOe within 2 and 300 K in order to evaluate the coercive field H_c, and saturation magnetization M_s. The coercive fields at positive and negative sides of the magnetic field axis were determined by linear regression of the magnetization data around the interceptions of the hysteresis loop with the field axis. H_c was defined as $H_c = (|H_c^+| + |H_c^-|)/2$, and the shift of the hysteresis loop along the field axis as $H_s = (|H_c^+| - |H_c^-|)/2$. In order to study H_s, hysteresis loops were recorded after field cooling (FC) the sample from 250 K down to the final measuring temperature under an applied magnetic field of 10 kOe.

The thermal dependence of the magnetization was measured after zero field cooling (M_{ZFC}) and field cooling (M_{FC}) the samples. These curves were collected using the following protocol: the sample was cooled down from 300 to 2 K in zero magnetic field, then a static magnetic field of 50 Oe was applied and M_{ZFC} was recorded while the sample was warmed up from 2 to 300 K. Then, the sample was again cooled down to 2 K under 50 Oe and M_{FC} was collected while rewarming up to 300 K.

Magnetization relaxation was measured after field cooling the sample under 50 Oe from room temperature down to each measuring temperature, switching off the field and then recording magnetization decay as a function of time at zero field and several temperatures.

Results and discussion

Structural characterization and sample composition

TEM images for R1, R2 and R3 show spherically shaped particles that tend to self-assemble in a hexagonal close-packing (see Figure 1). Figure 1 also shows the regularity and good monodispersity of the NPs for R1 and R3 and a wider size distribution for R2. The presence of the oleic acid coating at the particle surface prevents particle aggregation and keeps them a few nanometers apart from each other. The particle size distributions for the three samples were determined from TEM images and the resultant histograms (see Figures S1a, S1b and S1c in the Supporting Information) were fitted to log-normal distributions with the mean particle sizes (D_{TEM}) and unitless standard deviations (σ) indicated in Table 1. Interestingly, although R1, R2 and R3 samples were prepared using different reactants and protocols, all of them consist of NPs with similar morphology and size distributions which facilitates the comparison of their magnetic properties. Figures 1d, 1e and 1f show HRTEM images for samples R1, R2 and R3, respectively. R1 NPs are single crystal domains almost free of crystallographic defects up to the particle surface. In contrast, NPs of sample R3 show much poorer crystal quality with several in-volume defects and domain boundaries between randomly oriented smaller crystal domains that add up to form particles in a kind of crystallite aggregate (see Figure S2b, Supporting Information). NPs of R2 exhibit higher crystal quality than those of R3 but still not being completely free of crystallographic deffects and some of them even having about two non-coherent crystal domains randomly distributed throughout the particle (see Figure S2b and S3, Supporting Information).

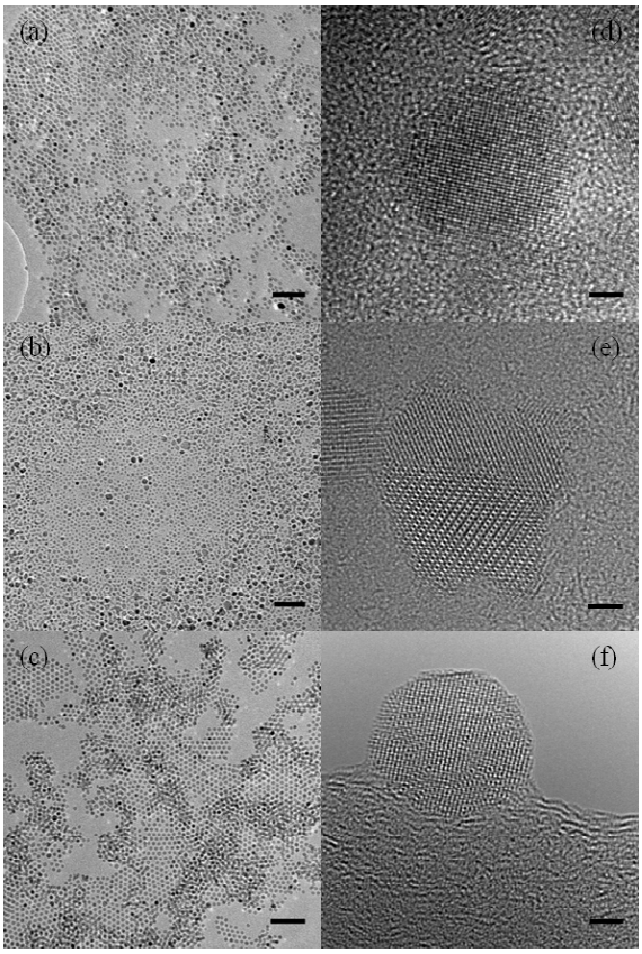

Figure 1. TEM images of $CoFe_2O_4$ NPs: (a) R1, (b) R2, (c) R3. HRTEM images of $CoFe_2O_4$ NPs: (d) R1, (e) example of a particle from R2 sample showing two crystal domains inside, (f) R3. Scale bars in (a), (b), (c) correspond to 85 nm and in (d), (e), (f) to 2nm.

All samples appear to be a single chemical phase of cobalt ferrite as ICP-OES analyses indicate an atomic Co:Fe ratio close to 1:2 in all cases, and no core-shell structures are observed by HRTEM. In the case of sample R3 (the most crystal defective particles), spatially resolved EDX and EELS analyses have also corroborated the homogenity of the composition up to the particle surface (see Figures S4, S5, S6, S7 and S8, Supporting Information) and discarded the existence of other CoFe-based phases.

The XRD spectra for R1, R2 and R3, which are shown in Figures S9a, S9b and S9c in the Supporting Information, respectively, have been indexed to an inverse spinel structure corresponding to stoichiometric $CoFe_2O_4$ without any significant traces of other phases. Using the Debye-Scherrer equation applied to the [400] reflection, the mean sizes (D_{XRD}) of the crystal domains have been determined for the three samples (see Table 1). D_{TEM} and D_{XRD} values are in perfect agreement for sample R1, as these NPs are crystal monodomains. In contrast, D_{XRD} is about four times smaller than D_{TEM} for R3 NPs in accordance with the crystal multidomain character of those highly defective particles. Finally, D_{XRD} is just slightly smaller than D_{TEM} for R2 indicating the existence of some crystallographic defects within the volume of some of the particles.

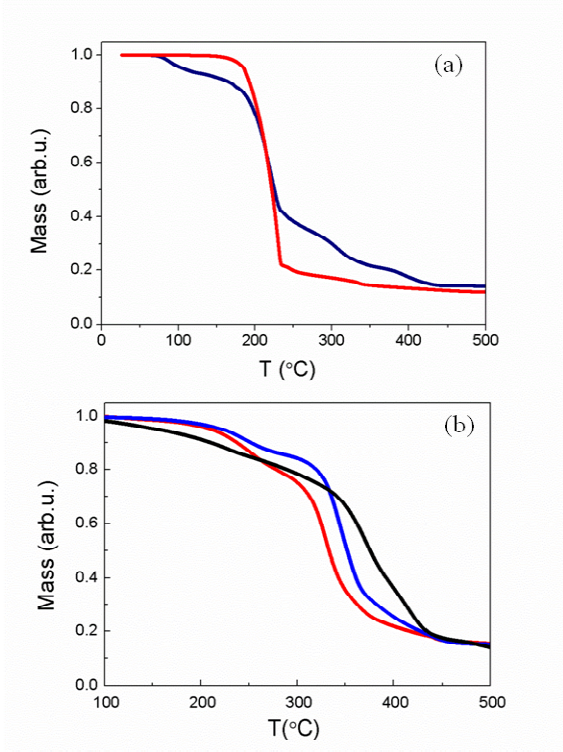

Figure 2. (a) TGA curves of Fe^{3+}-acetylacetonate (red solid line) and Co^{2+}-acetylacetonate (blue solid line). (b) TGA curves of Fe^{3+}-oleate (red solid line), Co^{2+}-oleate (black solid line) and the mixed-metal $Co^{2+}Fe_2^{3+}$-oleate (blue solid line).

Mechanisms of particle growth

The different size and crystallinity of the samples R1, R2 and R3 are intrinsically related to both the decomposition temperatures of the reactants involved in the reactions and reaction steps. While for the synthesis of R1 and R3 metal organic precursors are $Fe(acac)_3$ and $Co(acac)_2$,[15-21] for R2 they are the corresponding Fe and Co oleates.[17-19]

Typically, the synthesis of $CoFe_2O_4$ NPs by thermal decomposition of acetylacetonates as metal organic precursors is divided into two main steps.[20,21] First, the reaction mixture is kept 2 h at 200ºC. In this step Fe and Co acetylacetonates decompose at about 200 ºC (see Figure 2a) to form a polynuclear mixed-metal $Co^{2+}Fe_2^{3+}$-oleate that also starts to decompose yielding the nucleation of the NPs. After that, the reaction mixture is heated up and kept at boiling temperature, where the intermediate metal complex decomposes completely and the growth of the NPs takes place. As pointed out by LaMer,[23] one of the crucial aspects to synthesize monodisperse NPs relies on the fact that nucleation and growth processes must occur at different temperatures, as happens in the syntheses of samples R1 and R3.[22,23] In addition, the final contents of Fe and Co in both R1 and R3 samples are stoichiometric (see Table 1).

Despite the narrow distribution of particle sizes and stoichiometric composition of both samples, R3 shows a much more defective crystal structure related to a partial coalescence of smaller subunits (crystallite cores) rather than a uniform growth by diffusion.[22] This is probably due to the absence of 1,2-hexadecanediol in the R3 reaction and the specific role of this reactant: it enhances the decomposition of the organic precursors to form a polynuclear mixed-metal complex, thus homogenizing the growth of the NPs by diffusion.

On the other hand, R2 shows a broader particle size distribution having also a slight excess of Fe content and lower crystallinity than sample R1 (see Table 1 and S1b, Supporting Information). These results can be attributed to the different decomposition rates of Fe and Co oleates, since in this case an intermediate mixed-metal complex is not formed and nucleation and growth of the NPs go on from the parallel decompositions of the two oleates.[19] This is clear from Figure 2b where TGA curves corresponding to Fe^{3+}-oleate and Co^{2+}-oleate are shown. TGA curve for mixed-metal (Co^{2+}-Fe^{3+})-oleate has also been included for comparison in Figure 2b. Two different weight-loss rates are observed for Fe^{3+}-oleate. The first appears between 200 and 250 ºC and corresponds to the partial dissociation of the complex by elimination of CO_2.[24] In this first step there is a weight loss of a 25% associated with the loss of one oleate ligand. The second jump in the TGA curve (50% of weight loss between 300 and 350 ºC) corresponds to the loss of the two remaining oleate ligands yielding the final product. In contrast, Co^{2+}-oleate shows a constant loss-weight rate between 200 and 500 ºC (85% of weight loss), suggesting the progressive loss of the two oleate ligands.

Crystal quality and magnetic glassy behaviour

The different crystal quality of the samples is also reflected on the magnetization hysteresis loops shown in Figure 3 and on the values of M_s and H_c obtained from them. On one hand, for the conventional sample R1 at 5 K, M_s =77 ± 2 emu/g and H_c =15.6 ± 0.1 kOe, both values being in agreement with those reported elsewhere for high magnetic quality Co-ferrite NPs.[16,18] We note that the expected bulk value at low temperature is M_s = 475 emu cm^{-3} (80 emu g^{-1}).[6] On the other hand, R2 shows a slight decrease in both quantities (see Table 1) as a consequence of the hindering effect that the crystal defects, domain boundaries and the existence of local anisotropy axes associated with crystal domains within the particles may have on the long-range ferrimagnetic order. In any case, this effect has a very limited impact since the hysteresis loops of samples R1 and R2 look very much the same and highly resemble that expected for bulk $CoFe_2O_4$. In contrast, this degradation of the ferrimagnetic order is much more evident for R3, where the hysteresis loop at 5 K is totally different from the former curves for R1 and R2, resembling those of frustrated and disordered magnets, such as random anisotropy or cluster glass systems.[1] We attribute this behavior to the crystalline multidomain nature of the R3 NPs, where ferrimagnetic order tends to be arranged along the local magnetocrystalline anisotropy axes yielding magnetic multidomain NPs, in contrast with the single magnetic domains observed on high crystal quality Co-ferrite particles of similar size, as is the case of R1 and in some extent even R2. Moreover, frozen spins by magnetic frustration and local anisotropy axes at the crystal domain boundaries are known to give both a significant high-field linear contribution to the magnetization and hysteresis loops with high irreversibility (the hysteresis loops close at the highest applied magnetic field).[1]

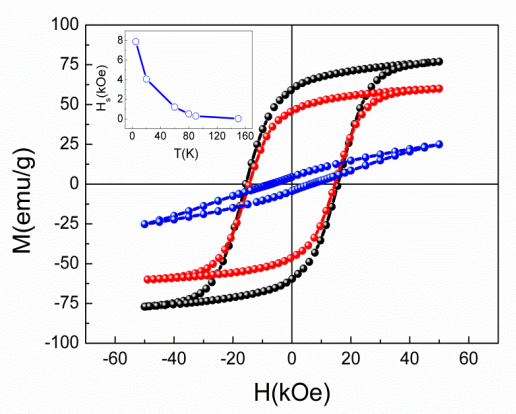

Figure 3. Hysteresis loops of Co-ferrite NPs synthesized following different methods: R1 (black spheres), R2 (red spheres), R3 (blue spheres). Inset: Temperature dependence of the horizontal loop shift, H_s, after field cooling sample R3 under 10 kOe from 250 K down to the measuring temperature.

Consequently, the saturation magnetization value of 25 emu/g at 5 K indicated in Table 1 for R3 -which is about one third of that of R1- arises mainly from the spins inside the core of the crystal domains, since those spins are the only ones that keep a ferrimagnetic-like ordering. This suggests that the high magnetic frustration present in R3 NPs is due to their crystalline multidomain structure (see Figure 1f). In addition, a large shift, H_s, of the hysteresis loop along the magnetic field axis is observed after cooling the particles down to about 80 K under 10 kOe, as shown in Figure S10 in Supporting information. The temperature dependence of H_s is displayed in the inset of Figure 3. Note that the cooling field of 10 kOe is smaller than the irreversibility field below 80 K, so this horizontal shift of the loops may not correspond to a true exchange bias phenomenon,[25] but just to minor loops of the hysteresis loop,[26] as expected when a ferro/ferrimagnet is not saturated under the maximum applied magnetic field.

A further insight in the strong reduction of M_s at low temperature may be gained by evaluating the distribution of the magnetic moments of the crystal domain cores with ferrimagnetic-like order, from the magnetization curves in the superparamagnetic (SPM) regime. In the SPM regime, crystal anisotropy barriers are overcome by thermal excitation so that ferrimagnetic-like cores in the crystal domains magnetize following the applied magnetic field. Then, SPM magnetization curves can be fitted by a log-normal distribution $P(m)$ of Langevin functions $L(x)$ plus a linear contribution to the magnetization, $\chi_p H$, coming from the highly frustrated spins at crystal domain boundaries and particle surface, as[27]

$$M(H,T) = M_C \frac{\int m P(m) L(mH/k_B T)\, dm}{\int m P(m)\, dm} + \chi_p H \qquad (1)$$

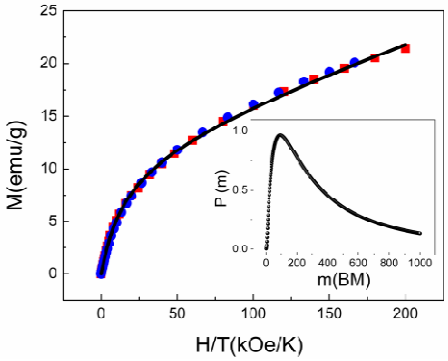

Figure 4. Isothermal magnetization curves for sample R3 in the superparamagnetic regime, measured at 250 K (red squares) and 300 K (blue circles), as a function of H/T. Black solid line corresponds to the fit of the data to Equation (1). Inset: Magnetic moment distribution of the ferrimagnetic-like crystallites obtained from the fit of the magnetization curves to Equation (1).

Where m is the magnetic moment per ferrimagnetic-like core, k_B is the Boltzmann constant, M_C is the mean value of the contribution of the ferrimagnetic-like cores to the saturation

magnetization and χ_p is a paramagnetic susceptibility. In the case of R3 NPs, SPM regime is reached above about 200 K, so we used isothermal magnetization curves at 250 and 300 K, scaled in a H/T plot, to perform this fitting (see Figure 4).

The fitted $P(m)$ distribution, shown in the inset to Figure 4, can be transformed in the distribution of magnetic domain sizes by assuming the $CoFe_2O_4$ bulk value of 475 emu cm^{-3} (80 emu g^{-1}) for the specific magnetization of the ferimagnetic-like crystallite cores.[6] The mean size of those crystallite magnetic domains and the value of the standard deviation are 1.9 nm and 0.4 nm, respectively, in very good agreement with crystalline features in HRTEM images (see Figure S2c, Supporting Information) and $D_{XRD} = 2.1 \pm 0.6$ nm (Table 1).

Additionally, the mean saturation magnetization of the ferrimagnetic-like cores deduced from this fitting is $M_C = 28.5$ emu/g, which is in quantitative agreement with the value obtained from the hysteresis loop at 5 K and 5 T (25 emu/g), temperature at which frustrated spins are essentially frozen so that the major contribution to the hysteresis loop comes from the ferrimagnetic-like cores.

This demonstrates the consistency of the estimation of the distribution of ferrimagnetic-like cores at the crystallite domains by fitting the magnetization curves in the SPM regime.

In addition, M_{ZFC} and M_{FC} curves, shown in the inset to Figure 5, provide further evidence of the high magnetic frustration existing among ferrimagnetic-like crystallites in R3 NPs at low temperature.

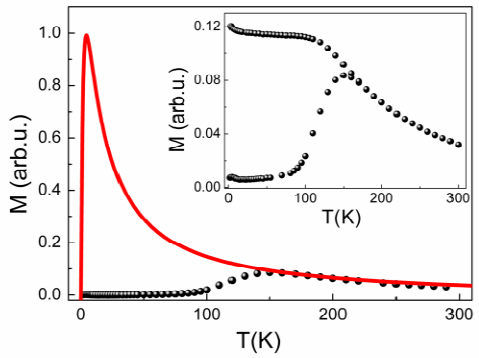

Figure 5. M_{ZFC} for R3 (black spheres). The solid red line represents M_{ZFC} curve calculated from Equation (2) with the distribution of magnetic moments for the ferrimagnetic-like cores shown in the inset to Figure 4. Inset: M_{ZFC}-M_{FC} for R3.

There are significant differences between M_{ZFC} - M_{FC} curves for R3 and a conventional sample, such as R1 for example. First, the peak of the M_{ZFC} curve is located at a temperature (T_p=150 K) much lower than what is expected for Co-ferrite NPs of about 8 nm in size (see Table 1 and Figure S11, Supporting Information). Second, M_{FC} is almost constant below T_p indicating the existence of strong interactions between the magnetic domains and/or the onset of a highly frustrated magnetic state at T_p.[1] The latter is also supported by the rapid decrease of M_{ZFC} below T_p, suggesting the occurrence of a freezing process due to high magnetic frustration rather than a simple blocking of particle magnetizations as the system is cooled down from the SPM regime.[1]

Moreover, M_{ZFC} is also very different from what could be expected for the simple blocking process of the distribution of ferrimagnetic-like crystallites, $P(m)$, that we have found by fitting the magnetization curves in the SPM regime (see Figure 4). Figure 5 shows a comparison between experimental M_{ZFC} and the corresponding curve calculated from $P(m)$ assuming the bulk values for the anisotropy constant and specific magnetization of Co-ferrite[3] ($K_v = 20\times10^5$ erg cm^{-3} and $M_0 = 475$ emu cm^{-3},[6] respectively), and using the following expression based on the Gittleman model,[26] for the blocking process of an assembly of non-interacting particles:

$$\frac{M_{ZFC}(T)}{H} = \frac{1}{3k_BT}\int_0^{M_0V_p(T)} m^2P(m)dm + \frac{M_0}{3K_v}\int_{M_0V_p(T)}^{\infty} mP(m)dm \qquad (2)$$

Where $V_p(T) = 25k_BT/K_v$. The two curves only coincide in the SPM regime (see T_{irr}, Table 1) where magnetic correlations among ferrimagnetic-like crystallites are weak and the net magnetizations of the NPs are mostly dominated by thermal activation of the small magnetic domains inside each particle. However, below around T_p the two curves quickly diverge as the temperature decreases and the calculated M_{ZFC} develops a sharp peak at low temperature associated with the progressive blocking of the small ferrimagnetic-like crystallites. In contrast, experimental M_{ZFC} curve shows a quite pronounced reduction of the magnetization towards zero as the magnetizations of the ferrimagnetic-like crystallites become frozen in random directions due to frustrated magnetic interactions at the boundaries of the crystallite domains.

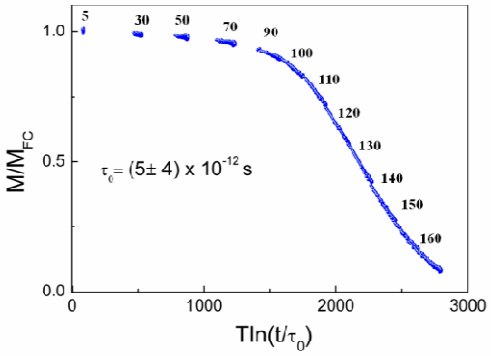

Figure 6. Scaling of the relaxation curves for R3, measured at several temperatures, with an attempt time of $\tau_0 = (5 \pm 4) \times 10^{-12}$ s.

The existence of high energy barriers originating at the magnetic frustration among crystallites constituting each particle has also been confirmed by measuring the time dependence of the relaxation of the magnetization. Relaxation

curves for R3 at several temperatures are analyzed in Figure 6 in terms of the $Tln(t/\tau_0)$ scaling where,[29] in order to make all the curves collapse onto a single master curve, the characteristic attempt time has been set to $\tau_0 = (5 \pm 4) \times 10^{-12}$ s and each curve has been divided by an arbitrary reference magnetization value that is pretty close to $M_{FC}(T)$.

The effective distribution of energy barriers, $f(E)$, calculated by numerical derivative of the scaling relaxation curve,[30] is shown in Figure 7. It is evident from Figure 7 that $f(E)$ is much broader and right-shifted to higher energies than both (i) the distribution of energy barriers of anisotropy corresponding to the volume distribution of the ferrimagnetic-like cores (see $P(m)$ in the inset to Figure 4); and (ii) the distribution of energy barriers of anisotropy corresponding to the particle size distribution obtained from TEM images (see S1c, in Supporting Information), thus indicating the key role of magnetic frustration among particle crystallites on determining the magnetic performance of those highly structural defective Co-ferrite NPs with stoichiometric composition.

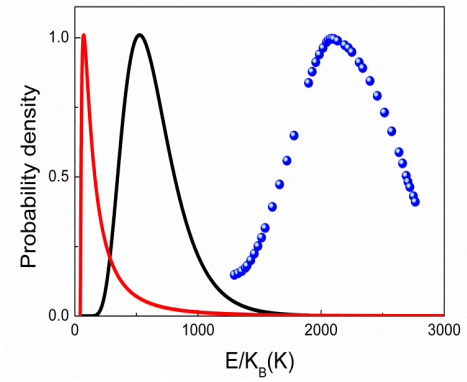

Figure 7. Comparison between the distribution of energy barriers of anisotropy corresponding to the volumes of the ferrimagnetic-like cores (red solid line) and the particle size distribution obtained from TEM images (black solid line). Those calculations were performed assuming the value of $K_v = 20 \times 10^5$ erg cm^{-3} for bulk Co-ferrite. The effective distribution of energy barriers calculated by the derivate of the scaling relaxation curve in Figure 6 (blue spheres) is also represented.

Conclusions

We have studied three samples of 8 nm Co-ferrite NPs synthesized by standard methods based on the thermal decomposition of metalorganic precursors.[13-19] Despite the facts that all three samples have very similar stoichiometry and distribution of particle sizes, and they are all even nominally single-phase $CoFe_2O_4$ according to the conventional methods of chemical and structural characterization performed, they show strongly sample-dependent magnetic properties, ranging from bulk-like ferrimagnetism to glassy magnetic behaviour. Interestingly enough, spatially-resolved composition characterization has discarded either the formation of core-shell structures or the presence of other chemical phases within the particles. This raises the question about the relevance that the actual crystallographic quality of the Co-ferrite NPs may have on their magnetic behaviour. As a matter of fact, crystallographic defects locally destabilize ferrimagnetic order yielding non-collinear arrangements of the spins that become frozen in a kind of glassy state at low temperature, largely spoiling the magnetic performance of the NPs. In particular, the paradigmatic situation corresponds to the presence of a number of small crystallite domains throughout the particles, which causes highly-frustrated ferrimagnetic-like cores that bring about much of the phenomenology typical of a glassy state. The existence of those small ferrimagnetic-like cores is also confirmed by fitting the magnetization curves in the SPM regime, leading to a distribution of magnetic volumes that is much smaller than the real size of the particles (D_{TEM}). These results highlight the key role of the crystal quality on the sample-dependent magnetic properties previously reported for Co-ferrite NPs. All in all, the structural defects in monodisperse, stoichiometric Co-ferrite NPs can be used as an additional nano-structuring procedure that tunes their final magnetic properties from bulk-like ferrimagnetism to glassy behaviour. In particular, Co-ferrite NPs with highly defective crystal structures show unexpected magnetic properties associated with an internal enhancement of the magnetic frustration that strongly reduces both the saturation magnetization and coercive field.

Acknowledgements

This work was supported by Spanish MINECO (MAT2011-23641, MAT2012-33037, MAT2013-48054-C2), Catalan DURSI (2014SGR220), and European Union FEDER funds (Una manera de hacer Europa) and MULTIFUN project no. 246479. C. Moya acknowledges Spanish MINECO for a Ph.D. contract (BES-2010-038075) and a three months stay at the ICMM/CSIC where the particles were synthesized. Dr. Nicolás Pérez (UB) is acknowledged for critical discussion of the results.

Notes and references

[a] Departament de Física Fonamental and Institut de Nanociència i Nanotecnologia (IN2UB), Universitat de Barcelona, Martí i Franquès 1, 08028 Barcelona, Spain
[b] Instituto de Ciencia de Materiales de Madrid, CSIC. C/Sor Juana de Inés de la Cruz 3, Campus de Cantoblanco. 28049 Madrid, Spain
[c] IMDEA Nanociencia, Ciudad Universitaria de Cantoblanco, C/ Faraday 9, E-28049 Madrid, Spain

† Electronic Supplementary Information (ESI) available: PDF material contains Particle size distributions of the samples, HRTEM of $CoFe_2O_4$ NPs with contrast colour, EDX and EELS experiments for sample R3, X-ray patterns of the samples, hysteresis loops after FC under 10 kOe from

250 K down to the final measuring temperature for sample R3 and $M_{ZFC} - M_{FC}$ curves for all the samples.

Notes and references

1 Batlle, X.; Labarta, A. *Journal of Physics D: Applied Physics*, 2002, **35**, R15.
2 Mejías, R.; Pérez-Yagüe, S.; Roca, A. G.; Pérez, N.; Villa nueva, A.; Cañete, M.; Mañes, S.; Ruiz-Cabello, J.; Benito, M.; Labarta, A.; Batlle, X.; Veintemillas-Verdaguer, S.; Morales, M. P.; Barber, D. F.; Serna, C. J. *Nanomedicine*, 2010, **5**, 397.
3 Pankhurst, Q. A.; Connolly, J.; Jones, S. K.; Dobson, J. *J. Phys. D. Appl. Phys.* 2003, ***36*,** R167.
4 Sun, C.; Lee, J. S. H.; Zhang, M. *Adv. Drug Deliv. Rev.* 2008, **60**, 1252.
5 Perez, J. M.; Josephson, L.; Weissleder, R. *Chembiochem*. 2004, **5**, 261.
6 Cullity, B. D.; Graham, C. D. *Introduction to Magnetic Materials*; 2011.
7 Pérez, N.; Guardia, P.; Roca, A. G.; Morales, M. P.; Serna, C. J.; Iglesias, O.; Bartolomé, F.; García, L. M.; Batlle, X.; Labarta, A. *Nanotechnology*. 2008, **19**, 475704.
8 Geshev, J. *J. Magn. Magn. Mater.* 2008, **320**, 600.
9 Leite, E. S.; Coaquira, J. A. H.; Viali, W. R.; Sartoratto, P.P.C.; Almeida, R. L. De Morais, P. C.; Malik, S. K. *J. Phys. Conf. Ser.* 2010, **200**, 072060.
10 Hou, Y. H.; Zhao, Y. J.; Liu, Z. W.; Yu, H. Y.; Zhong, X. C.; Qiu, W. Q.; Zeng, D. C.; Wen, L. S. *J. Phys. D. Appl. Phys.* 2010, **43**, 445003.
11 Peddis, D.; Cannas, C.; Piccaluga, G.; Agostinelli, E.; Fiorani, D. *Nanotechnology*. 2010, **21**, 125705.
12 Cedeño-Mattei, Y.; Perales-Pérez, O.; Uwakweh, O. N. C. *Mater. Chem. Phys.* 2012, **132**, 999.
13 Zhang, Y.; Yang, Z.; Zhu, B.-P.; Ou-Yang, J.; Xiong, R.; Yang, X.-F.; Chen, S. *J. Alloys Compd.* 2012, **514**, 25.
14 Gyergyek, S.; Makovec, D.; Kodre, A.; Arčon, I.; Jagodič, M.; Drofenik, M. *J. Nanoparticle Res.* 2009, **12**,1263.
15 Sun, S.; Zeng, H. *J. Am. Chem. Soc.* 2002, **124**, 8204.
16 Sun,S.; Zeng, H.; Robinson, D. B.; Raoux, S.; Rice, P.M.; Wang, S.X.; Li, *J. Am. Chem. Soc.* 2004, **126**, 273.
17 Bao, N.; Shen, L.; Wang, Y.; Padhan, P.; Gupta, A. *J. Am.Chem. Soc.* 2007, **129**, 12374.
18 Song, Q.; Zhang, Z. J. *J. Am. Chem. Soc.*. 2004, **126**, 6164.
19 Cabrera, L. I.; Somoza, Á.; Marco, J. F.; Serna, C. J.; Morales, M. P. *J. Nanoparticle Res.* 2012, **14**, 873.
20 Pérez, N.; López-Calahorra, F.; Labarta, A.; Batlle, X. *Physical Chemistry Chemical Physics.* 2011, **3**, 19485.
21 Guardia, P.; Pérez, N.; Labarta, A.; Batlle, X. *Langmuir*. 2010, **26**, 5843.
22 Tartaj, P.; Morales, M. P.; Veintemillas-Verdaguer, S.; González-Carreño, T.; Serna, C. J. *J. Phys. D. Appl. Phys.* 2003, **36**, R182.
23 LaMer, V. K.; Dinegar, R. H. *J. Am. Chem. Soc.* 1950, **72**, 4847.
24 Salas, G.; Casado, C.; Teran, F. J.; Miranda, R.; Serna, C. J.; Morales, M. P. *J. Mater. Chem.* 2012, 22, 21065.
25 Nogués, J.; Schuller. *JMM*. 1999, **192**, 203.
26 Batlle, X; Pérez N.; Guardia, P.; Iglesias, O.; Labarta, A.; Bartolomé, F.; García, L.M.; Bartolomé, J.; Roca, A.G.; Morales, M.P.; Serna, C.J. *J. Appl. Phys*. 2012, **109**, 07B524.
27 Bean, C. P.; Livingston, J. D. *J. Appl. Phys.* 1959, **30**, S120.
28 Gittleman, J.; Abeles, B.; Bozowski, S. *Phys. Rev. B*. 1974, **9**, 3891.
29 Labarta, A.; Iglesias, O.; Balcells, L.; Badia, F. *Phys. Rev. B*. 1993, **48**, 10240.
30 Iglesias, O.; Badia, F.; Labarta, A.; Balcells, L. *Zeitschrift für Phys. B Condens. Matter*. 1996, **100**, 17.

Table 1. Summary of the structural, microstructural, and magnetic parameters of the samples studied.[a]

Samples	D_{TEM} (nm)	σ [b]	D_{XRD} (nm)	Co:Fe (ICP-OES)	T_p (K)	T_{irr} (K)	M_s at 5K (emu/g)	M_s at 300 K (emu/g)	H_c at 5 K (kOe)	H_c at 300 K (kOe)
R1	7.8	0.12	7.7 (0.4)	1.0:2.0	280	290	77(2)	64(2)	15.6(0.1)	0.016 (0.01)
R2	7.2	0.25	6.9(0.5)	1.0:2.1	>300	>300	60(2)	47(2)	14.5(0.1)	0.084 (0.01)
R3	8.6	0.13	2.1(0.6)	1.0:2.0	150	170	25(1)	20(1)	6.8(0.2)	SPM[c]

[a]The values in parentheses indicate the experimental error of the data.
[b]Unitless standard deviation of the log-normal distribution.
[c]SPM stands for superparamagnetic.

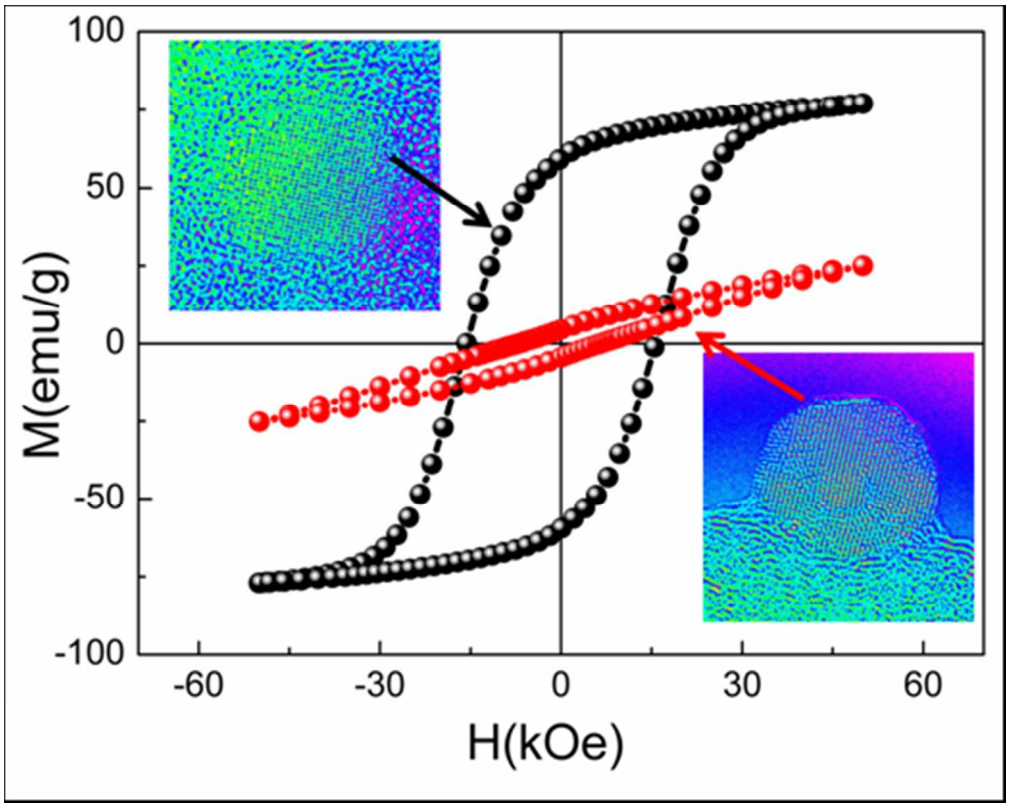

88x70mm (150 x 150 DPI)